Journal of Geophysical Research: Solid Earth

RESEARCH ARTICLE
10.1029/2018JB015973

Aqueous Fluid Connectivity in Subducting Oceanic Crust at the Mantle Transition Zone Conditions

Xingcheng Liu[1,2], Kyoko N. Matsukage[2,3], Yuan Li[1], Eiichi Takahashi[1,2], Toshihiro Suzuki[2], and Xiaolin Xiong[1]

[1]State Key Laboratory of Isotope Geochemistry, Guangzhou Institute of Geochemistry, Chinese Academy of Sciences, Guangzhou, China, [2]Magma Factory, Department of Earth and Planetary Sciences, Tokyo Institute of Technology, Tokyo, Japan, [3]Center for Fundamental Education, Teikyo University of Science, Uenohara, Japan

Abstract Experiments were performed at 17–19 GPa and 1000–1200 °C to determine the aqueous fluid-majoritic garnet-majoritic garnet dihedral angle $\theta_{grt\text{-}grt}$ in a basalt-H_2O system. The results show that the $\theta_{grt\text{-}grt}$ is between 44 ± 2° and 55 ± 3°, decreasing with increasing pressure and temperature. These new data combined with previous data obtained in the aqueous fluid-olivine and aqueous fluid-garnet systems suggest that connected network of aqueous fluids can form in the peridotite part of the subducting slab but may not form in a cold subducting oceanic crust at pressures below 14 GPa. Therefore, aqueous fluids formed by dehydration of a cold slab could be trapped as interstitial fluids in the oceanic crust and transported into the deep mantle. However, at the mantle transition zone (MTZ) conditions, aqueous fluids trapped previously and/or formed lately by the breakdown of hydrous minerals can percolate through the oceanic crust and hydrate the MTZ, providing an important mechanism for the MTZ hydration. Furthermore, aqueous fluids formed by mineral dehydration in a hot slab are readily lost into the mantle wedge at shallow depth, due to low dihedral angles ($\theta < 60°$) of the subducting oceanic crust, resulting in less water available to hydrate the MTZ. The distinct contribution of the cold slab and the hot slab to the MTZ hydration may cause water heterogeneity in the MTZ.

Key Points:
- Aqueous fluid-majoritic garnet-majoritic garnet dihedral angle is between 44° and 55° at 17-19 GPa and 1000-1200°C, decreasing with increasing *P* and *T*
- Aqueous fluids formed by breakdown of hydrous minerals can percolate through the subducting slab and hydrate the mantle transition zone
- Cold slab may be more efficient than hot slab in deep water cycle and hydration of the mantle transition zone

Supporting Information:
- Supporting Information S1
- Table S1

Correspondence to:
X. Liu and Y. Li,
liuxingcheng@gig.ac.cn;
yuan.li@gig.ac.cn

Citation:
Liu, X., Matsukage, K. N., Li, Y., Takahashi, E., Suzuki, T., & Xiong, X. (2018). Aqueous fluid connectivity in subducting oceanic crust at the mantle transition zone conditions. *Journal of Geophysical Research: Solid Earth*, *123*, 6562–6573. https://doi.org/10.1029/2018JB015973

Received 17 APR 2018
Accepted 8 JUL 2018
Accepted article online 16 JUL 2018
Published online 29 AUG 2018

1. Introduction

The distribution and cycle of water in Earth's interior is one of the most critical factors controlling Earth's geochemical and geodynamical evolution (e.g., Hirschmann, 2006). A small amount of water can significantly affect the properties of Earth's mantle material, such as solidus, viscosity, electrical conductivity, and seismic velocity (e.g., Bolfan-Casanova, 2005; Dixon et al., 2004; Hirth & Kohlstedt, 1996; Karato, 2011; Karato & Jung, 1998; Kelbert et al., 2009; Keppler, 2017). Our knowledge of the water cycle in subduction zones has been significantly improved by extensive studies on the stability of hydrous minerals at high *P-T* conditions (e.g., Frost, 2006; Kawamoto, 2006; Ohtani, 2015, and references therein), and it is now generally believed that the subducting slab can bring a significant amount of water to the mantle transition zone (MTZ) and even to the lower mantle. It has also been suggested that aqueous fluids can be formed due to the breakdown of hydrous minerals in the subducting slab, and these aqueous fluids may eventually hydrate the overlying mantle including the MTZ (e.g., Bolfan-Casanova, 2005; Frost, 2006; Hirschmann, 2006; Karato et al., 2013; Kawamoto, 2006; Ohtani, 2005, 2015; Schmidt & Poli, 1998). However, whether the aqueous fluids formed due to the breakdown of hydrous minerals can flow on the grain edges at deep subduction conditions has received little attention. If the aqueous fluids cannot form interconnected network, they could be trapped physically in the subducting slab and may not be available for the hydration of the overlying mantle.

In the past 30 years, it has been well established that the dihedral angle θ provides important information on the connectivity of aqueous fluids in the Earth's interior (Brenan & Watson, 1988; Holness, 1993, 2006; Matsukage et al., 2017; Mibe et al., 1999, 2003; Ono et al., 2002; Watson, 1982; Watson & Brenan, 1987; Watson et al., 1991; Watson & Lupulescu, 1993; Yoshino et al., 2002, 2007). The dihedral angle θ is the angle formed at the junction of two solid grains in textural equilibrium with a fluid phase. A θ value of less than 60° would mean that even a small amount of fluids can fill the channels between mineral grains and efficient percolation is possible. However, when the θ value is above 60° or the fluid fractions are very low, fluids can only form disconnected pockets and efficient percolation is not possible. It should be noted that dihedral angle theory is strictly valid for an isotropic and static (nondeforming) system. Mineral anisotropy,

Table 1
Major Element Compositions of Starting Materials (in Weight Percent)

Major element oxides	Starting material[a]		JB-2[b]	MORB[c]
	SM3.5	SM2.1		
SiO_2	47.22	49.63	53.25	50.47
TiO_2	1.05	1.10	1.18	1.68
Al_2O_3	12.98	13.64	14.64	14.70
FeO	8.85	9.30	9.98	10.43
Fe_2O_3	2.95	3.10	3.33	—
MnO	0.19	0.20	0.21	0.18
MgO	11.93	9.01	4.62	7.58
CaO	8.78	9.23	9.90	11.39
Na_2O	1.81	1.90	2.04	2.79
K_2O	0.37	0.39	0.42	0.16
P_2O_5	0.09	0.09	0.10	0.18
H_2O	3.50	2.10	—	—
total	99.70	99.69	99.67	99.56
Mg#	64.53	56.65	38.45	56.68

[a]Two different starting mixtures were prepared by mixing a JB-2 basalt and brucite. [b]The major element composition of the JB-2 basalt. [c]The average major element composition of mid-ocean ridge basalt (MORB) from Gale et al. (2013) is listed for comparison.

inhomogeneous mineral distribution, or deformation at the grain boundary scale could complicate the interpretation of permeability.

In order to constrain the connectivity of aqueous fluids in Earth's interior, a number of studies have measured the dihedral angles of aqueous fluid-mineral-mineral at *P-T* conditions relevant for the crust and the upper mantle (Brenan & Watson, 1988; Holness, 1993; Holness & Graham, 1991; Matsukage et al., 2017; Mibe et al., 1998, 1999, 2003; Ono et al., 2002; Wanamaker & Kohlstedt, 1991; Watson et al., 1991; Watson & Brenan, 1987; Yoshino et al., 2002, 2007). For example, Watson et al. (1991), Mibe et al. (1998, 1999), and Yoshino et al. (2007) determined systematically the effects of *P-T* on the aqueous fluid-olivine-olivine dihedral angle $\theta_{oliv\text{-}oliv}$ up to 1200 °C and 13 GPa, and these authors found that increasing *P-T* can effectively decrease the $\theta_{oliv\text{-}oliv}$ from above 60° to significantly below 60°, indicating efficient percolation of aqueous fluids in the deep upper mantle. Ono et al. (2002) measured the dihedral angle in the H_2O-pyrope system at 900–1200 °C and 4–13 GPa. They found that the dihedral angle $\theta_{grt\text{-}grt}$ increases with increasing pressure up to 9 GPa, and at pressures of above 9 GPa the $\theta_{grt\text{-}grt}$ is greater than 60° if the temperature is below 1000 °C. Matsukage et al. (2017) measured the dihedral angles of clinopyroxene and garnet in the basalt-H_2O system at 1000 °C and 4–16 GPa, in which they found that $\theta_{cpx\text{-}cpx}$ remains around 60° but $\theta_{cpx\text{-}grt}$ is always higher than 60°. They also found that $\theta_{grt\text{-}grt}$ increases from 46° at 4 GPa to 66° at 12 GPa, although it showed a weak decreasing trend at pressures higher than 12 GPa. Therefore, Ono et al. (2002) and Matsukage et al. (2017) concluded that a part of the aqueous fluids formed from the breakdown of hydrous minerals may be trapped in the subducting oceanic crust and transported into the deep mantle.

However, despite significant efforts made by previous authors, our understanding of the connectivity of aqueous fluids in the subducting oceanic crust is still heavily hampered by the lack of experiments at MTZ pressures. Previous studies show that the subducting basaltic crust consists mainly of majoritic garnet when the pressure is higher than 16 GPa (e.g., Aoki & Takahashi, 2004; Irifune et al., 1986; Matsukage et al., 2017; Okamoto & Maruyama, 2004). Determining the dihedral angle of aqueous fluid-majoritic garnet-majoritic garnet and the effects of *P-T* are thus required to understand the connectivity of aqueous fluids in the subducting oceanic crust at very high pressures, which in turn could be very important to our understanding of the hydration of the Earth's mantle including the MTZ. We therefore performed experiments at 17–19 GPa and 1000–1200 °C on a hydrous basaltic system to determine the aqueous fluid-majoritic garnet-majoritic garnet dihedral angles. Our results in conjunction with previously determined dihedral angles are used to discuss the water cycle in subduction zones and the hydration of the MTZ.

2. Experimental Techniques

2.1. High *P-T* Experiments

Two different starting materials, which were prepared by mixing a natural JB-2 basalt (a reference basalt distributed by the Geological Survey of Japan) and brucite ($Mg(OH)_2$) reagent with different mass proportions, were used in this study. We choose natural basalt as the starting material because it would reduce the effect of mineral composition on the constrained fluid connectivity in subducting oceanic crust. Each starting material was ground under acetone over an hour for homogeneity and then heated in an oven at 110 °C overnight to remove moisture. The major element compositions of the two different starting materials and the JB-2 basalt are listed in Table 1. The water content of the two different starting materials is about 2.1 and 3.5 wt.%, respectively (Table 1).

A double capsule technique was used to encapsulate the sample material. The starting material was loaded into an inner Au capsule (1.3-mm O.D.; 1.1-mm I.D.; 1.5-mm length), which was then loaded into an outer Pt capsule (1.6-mm O.D.; 1.4-mm I.D.; 2.5-mm length). The sample was kept at oxygen fugacity of the Ni-NiO buffer, by loading a mixture of NiO + Ni + $Ni(OH)_2$ powder in the space between the inner Au and the outer Pt capsule. In addition, very thin Pt foil was used to wrap the inner Au capsule to avoid any potential reaction

Table 2
Summary of Experimental Conditions and Products

Run no.	T (°C)	P (GPa)	Duration (hr)	Starting material	Run products	Median angle ($\theta_{grt\text{-}grt}$)	N_{total}	N_{type1}
DHL-1	1000	17	24	SM3.5	grt (81), sti (10), Fe–Ti (4), Ti–CaPv (3), fl	55 (3)	169	131
DHL-4	1200	17	24	SM3.5	grt (88), sti (8), Ti–CaPv (3), fl	47 (2)	199	160
DHL-13	1000	18	24	SM2.1	grt (77), Ti–CaPv (1), Fe-Ti (5), hol (2), sti (14), fl	54 (2)	237	162
DHL-5	1000	19	24	SM3.5	grt (67), Al-phase D (18), Ti–CaPv (3), rwd (5), hol (3), sti (4), fl	52 (3)	183	138
DHL-19	1100	19	24	SM3.5	grt (75), Fe–Ti (4), CaPv (6), rwd (4), hol (2), sti (9), fl	50 (3)	166	114
DHL-10	1200	19	13	SM3.5	grt (82), sti (8), Ti–CaPv (3), CaPv (1), rwd (3), fl	44 (2)	241	162

Note. N = number of measurements. Values in parentheses of angles denote the error of true dihedral angle. Values in parentheses of minerals denote the proportion of run products. grt = majoritic garnet; sti = stishovite; Fe-Ti = Fe-Ti oxyhydroxide; Ti-CaPv = Ti-rich Ca-perovskite; fl = fluid; hol = K-hollandite; rwd = ringwoodite; Al-phase D = Al-rich phase D; CaPv = Ca-perovskite. The starting material in run DHL-13 contains 2.1 wt.% water and the others contain 3.5 wt.%.

between the buffer materials and the inner Au capsule. Both the inner Au capsule and the outer Pt capsule were sealed by arc welding.

Six experiments were performed at pressures of 17–19 GPa and temperatures of 1000–1200 °C, using a 2,500-t Kawai-type multianvil apparatus at the Tokyo Institute of Technology. Tungsten carbide anvils with truncations of 5-mm edges were used in combination with a Cr-doped MgO octahedral pressure medium with 10-mm edge length. Pyrophyllite gaskets were used to support the anvil flanks. Cylindrical $LaCrO_3$ was used as a heater and an MgO sleeve was used to separate the heater from the sample capsule. All the experiments were first pressurized to the target pressure at room temperature and then were heated to the desired temperatures at a rate of 50 °C/min. The pressure was calibrated based on the phase transitions of Bi (I–II), ZnS, GaAs, and GaP at room temperature and of SiO_2 (coesite-stishovite), olivine (α-β and β-γ), and $MgSiO_3$ (ilmenite-perovskite) at 1600 °C (Katsura, 2004; Matsuzaka et al., 2000; Zhang et al., 1996). The temperature was measured using a 0.125-mm diameter $W_{95}Re_5$-$W_{74}Re_{26}$ type-C thermocouple. The pressure and temperature uncertainties are thought to be better than 1 GPa and 50 °C. The run durations ranged from 13 to 24 hr depending on the run temperature. All the experiments were quenched by switching off the electricity to the heater. The recovered samples were mounted in epoxy resin and carefully polished to prevent the mineral grain plucking.

2.2. Analytical Techniques

The polished samples were analyzed with a focused beam on a JEOL-JXA8530F electron microprobe at the ELSI, Tokyo Institute of Technology. The operation voltage was 15 kV, and the beam current was 10 nA to measure the major element compositions of the silicate minerals. The standards employed were wollastonite (Ca, Si), hematite (Fe), periclase (Mg), corundum (Al), albite (Na), aduralia (K), rutile (Ti), Cr_2O_3 (Cr), bunsenite (Ni), and tephroite (Mn). The counting times were 20 s on peak and 10 s for background for all the elements except for Na and K (10 s on peak and 5 s for background). A focused beam was used in the analysis. The secondary electron and backscattered electron photomicrographs of the samples, with a resolution of 542 dpi, were also obtained for further dihedral angle measurements. The magnification was about 3,500–10,000 depending on the pore size. The dihedral angles were measured using the protractor provided in Scion Image, an image analysis software developed by National Institute of Health for Windows. More than 100 measurements were conducted for each sample in the random cross section at the capsule hotter part. The measurement uncertainty for each sample is estimated to be within ±5°. The median of the apparent angle distribution is adopted as the true dihedral angle (Jurewicz & Jurewicz, 1986).

3. Results

3.1. Run Products

A summary of the experimental conditions and products is given in Table 2. The resulting phase assemblages consist of 67–88% garnet and various proportions of stishovite (4–14%) + Ca-perovskite (1–5%) ± K-hollandite (0–3%) ± ringwoodite (0–5%) ± hydrous phase (Fe-Ti oxyhydroxide or Al-rich phase D; 0–18%), based on mass balance calculation (the compositions of run products are presented in Table S1 in the supporting information). The hydrous Fe-Ti oxyhydroxide and Al-rich phase D are only present in the runs

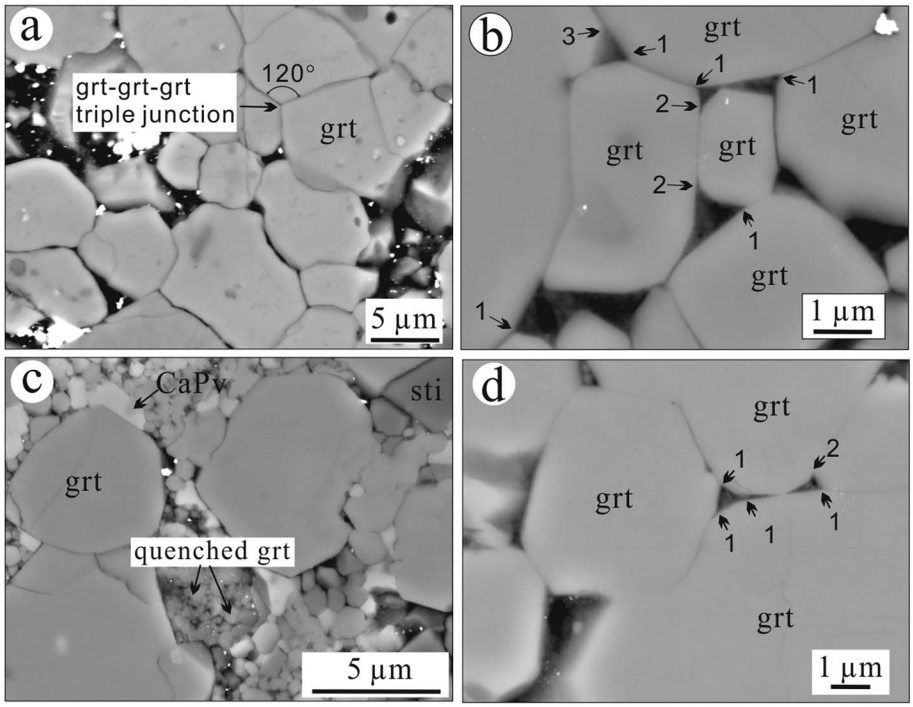

Figure 1. Backscattered electron images of representative run products: (a) Run DHL-13 at 18 GPa and 1000 °C; (b) run DHL-10 at 19 GPa and 1200 °C; (c) run DHL-5 at 19 GPa and 1000 °C; (d) run DHL-4 at 17 GPa and 1200 °C. grt = majoritic garnet; sti = stishovite; CaPv = Ti-rich Ca-perovskite. The black areas are grain junctions that were filled with aqueous fluids at run conditions. Note that, as shown in (a), the garnet grains meeting at approximately 120° triple junctions indicates textural equilibrium at run conditions. The arrows in (b) and (d) point to three different types of dihedral angles at aqueous fluid-garnet-garnet triple junctions (see text for details). The arrow in (c) points to the garnet crystals precipitated from fluids during quench. Note that the big holes (larger than 5 μm) in a may be from grain plucking.

with temperatures below 1100 °C and will be reported in detail elsewhere. The grain sizes of the silicate minerals are mostly less than 10 μm. The representative backscattered electron images of run products are shown in Figure 1. The void space filled with epoxy between minerals, as shown in Figure 1, indicates the presence of free aqueous fluids at the experimental conditions.

The garnet crystals are usually larger than 2 μm (Figure 1). The major element compositions of the garnets are 42.55–45.62 wt.% SiO_2, 0.12–0.81 wt.% TiO_2, 15.48–18.32 wt.% Al_2O_3, 11.49–13.41 wt.% FeO, 0.24–0.26 wt.% MnO, 10.43–15.13 wt.% MgO, 7.70–13.80 wt.% CaO, 0.97–2.14 wt.% Na_2O, and trace amounts of K_2O, Cr_2O_3, and NiO (see Table 3). No compositional zoning was observed in garnet crystals from any individual run. Based on these compositions, the garnets are majoritic garnets, consistent with the results of previous studies performed at similar conditions (e.g., Aoki & Takahashi, 2004; Irifune et al., 1986; Matsukage et al., 2017; Okamoto & Maruyama, 2004). In addition, we found some small garnet crystals, which are distributed in the fluid void spaces (Figure 1). Compared to those garnet crystals, which are larger than 2 μm and are thought to be in equilibrium with the fluids during the run, these garnet crystals are smaller than 1 μm and generally have higher Al_2O_3 and CaO contents but lower SiO_2, MgO, and FeO contents. We believe that these small garnets are products precipitated from the fluids during quench.

In the recovered run products, mass balance calculations and electron microprobe analyses show that there is no noticeable iron loss from the sample to Au capsule. The recovered oxygen fugacity buffer materials were also carefully checked under the optical microscope immediately after opening the sample capsule. The results show that Ni, NiO, and water all were still present in the space between the inner Au capsule and outer Pt capsule.

3.2. Dihedral Angles

Since the fine-grained garnets (smaller than 1 μm) are the products precipitated from the aqueous fluids during quench, we only measured the apparent dihedral angles of the majoritic garnets that are in equilibrium

Table 3
Major Element Composition of Majoritic Garnet (Weight Percent)

Element Composition	Run no.					
	DHL-1	DHL-4	DHL-13	DHL-5	DHL-19	DHL-10
T (°C)	1000	1200	1000	1000	1100	1200
P (GPa)	17	17	18	19	19	19
N	24	13	15	10	6	18
SiO_2	43.98(0.43)	44.51(0.26)	42.55(0.61)	45.62(0.59)	43.57(0.78)	44.08(0.47)
TiO_2	n.a.	0.37(0.17)	0.81(0.40)	0.29(0.30)	0.12(0.05)	0.12(0.05)
Al_2O_3	15.48(0.55)	16.28(0.61)	18.02(0.62)	17.04(0.25)	18.25(0.94)	18.32(0.46)
FeO	13.27(0.73)	13.08(0.22)	11.49(4.11)	12.65(0.66)	12.48(2.36)	13.41(0.50)
MnO	0.26(0.04)	0.24(0.03)	0.24(0.06)	0.29(0.02)	0.26(0.04)	0.25(0.06)
MgO	14.91(0.47)	13.79(0.55)	10.43(0.87)	11.89(0.94)	15.13(0.89)	14.62(0.45)
CaO	9.48(0.65)	9.34(0.44)	13.80(4.22)	9.09(0.70)	7.93(1.26)	7.70(0.47)
Na_2O	1.27(0.19)	1.01(0.11)	1.62(0.22)	2.14(0.25)	1.27(0.31)	0.97(0.10)
K_2O	0.04(0.03)	0.04(0.03)	0.04(0.02)	0.03(0.03)	0.06(0.05)	0.03(0.03)
Cr_2O_3	0.02(0.02)	0.01(0.01)	0.02(0.02)	0.01(0.02)	0.02(0.02)	0.02(0.02)
NiO	0.01(0.01)	0.01(0.01)	0.02(0.02)	0.01(0.01)	0.01(0.01)	0.01(0.02)
Total	98.71(0.38)	98.69(0.28)	99.04(0.64)	99.05(0.52)	99.11(0.72)	99.53(0.48)

Note. N = number of analyses; n.a. = not analyzed. Number in the bracket corresponds to 1σ standard deviation.

with the fluids. We used the median value as the true dihedral angle for each sample, because the difference between the median of the observed apparent angles and the true angle is very small (less than one degree) if a large number of measurements are conducted. (Jurewicz & Jurewicz, 1986; Riegger & Vanvlack, 1960). The error of the true dihedral angle is based on a 95% confidence interval around the median as described in Stickels and Hucke (1964).

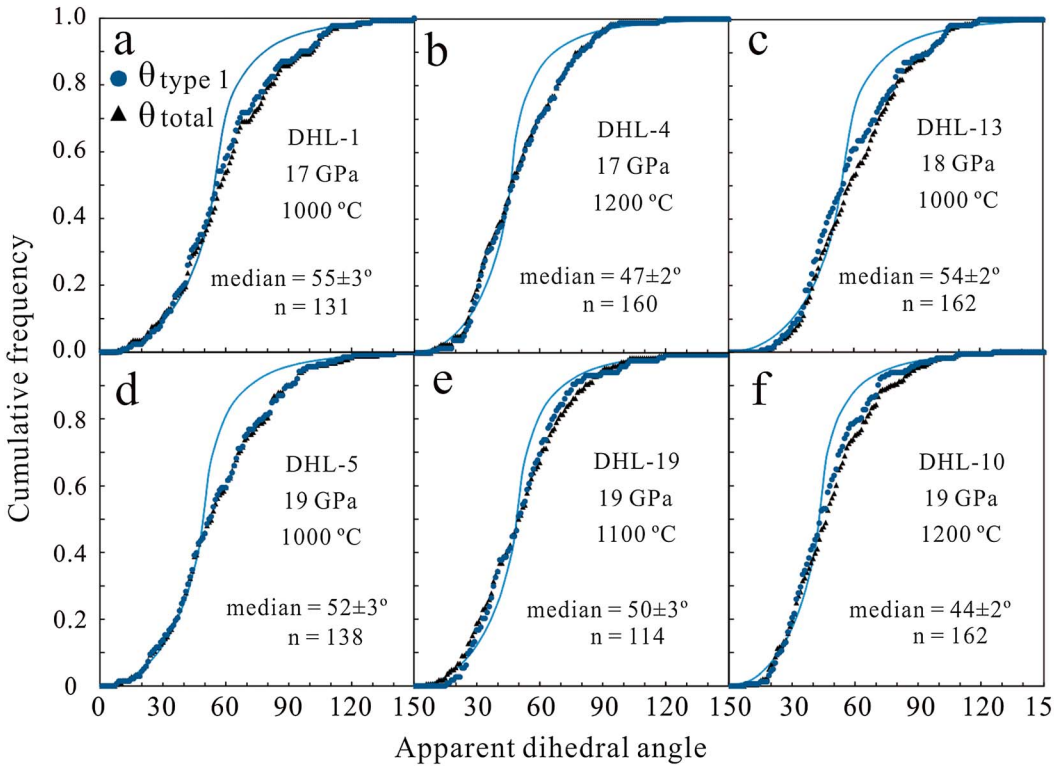

Figure 2. Cumulative frequency distributions for measured apparent dihedral angles at fluid-garnet-garnet triple junctions in this study. The theoretical cumulative frequency curves of true dihedral angles are also shown for comparison (solid blue curves). Note that the difference between Type 1 dihedral angles (blue circles) and the total dihedral angles (black triangles, Types 1–3) are very small. See text for details.

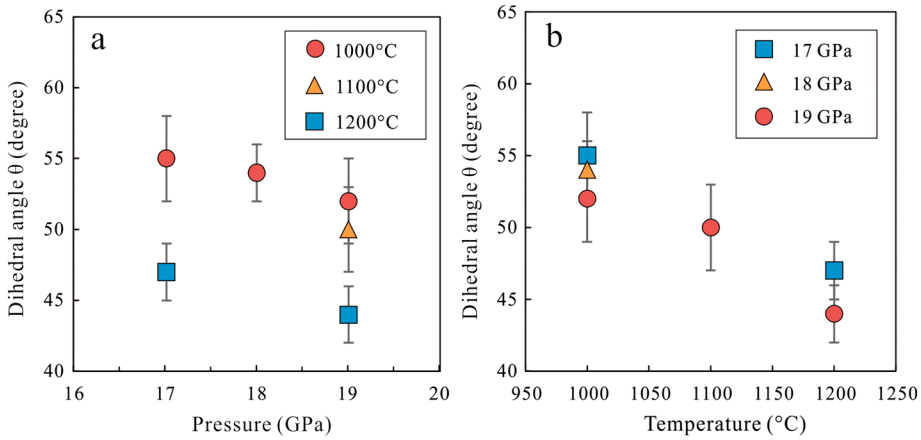

Figure 3. The aqueous fluid-majoritic garnet-majoritic garnet dihedral angle $\theta_{grt\text{-}grt}$ in the H_2O-basalt system decreases with increasing pressure (a) and temperature (b).

Previous studies show that silicate mineral-fluid interfaces frequently have faceted faces, which can potentially affect the connectivity of fluids (Yoshino et al., 2002, 2006). Yoshino et al. (2006) also suggested that the permeability of texturally equilibrated rocks with low fluid fraction in a faceting system would be significantly decreased. Therefore, in order to evaluate the degree and effect of faceting, we divided the dihedral angles into three different types, depending on the geometrical shape of pore space (see Figure 1). Type 1 dihedral angles are the angles between two smoothly curved interfaces, Type 2 are angles between one faceted interface and one smoothly curved interface, and Type 3 are angles between two faceted interfaces (see also Yoshino et al., 2002, and Mibe et al., 2003, for more details). The results show that the Type 1 dihedral angles are predominant, and the difference between Type 1 dihedral angles and the total dihedral angles (Types 1–3) are smaller than the experimental uncertainties (see Table 2 and Figure 2), indicating that the degree and effect of faceted interface are limited. This result is consistent with the observation in Yoshino et al. (2002) who concluded that the crystallographic control is significant only at large grain size (>5 μm) and that long run duration reduces the effect of faceting. In this study, we choose median value of only Type 1 dihedral angles as the true dihedral angle.

The cumulative frequency curves obtained from measurements of the apparent Type 1 and total dihedral angles are shown in Figure 2. The distribution of the apparent dihedral angles is broader than that of the theoretically calculated dihedral angles, as observed in previous studies (e.g. Matsukage et al., 2017; Mibe et al., 1998; Yoshino et al., 2002, 2007). Besides measurement uncertainty, the deviation could be also caused by different crystal orientations, which, however, may not have significant influence on the true dihedral angles within measurement uncertainty (Holness, 2006; Mibe et al., 2003; Ono et al., 2002). Table 2 and Figure 3 show that the determined aqueous fluid-majoritic garnet-majoritic garnet dihedral angle $\theta_{grt\text{-}grt}$ in this study is between 44 ± 2° and 55 ± 3°. As shown in Figure 3, $\theta_{grt\text{-}grt}$ is negatively correlated with both temperature and pressure, that is, a higher temperature and/or pressure yield a smaller $\theta_{grt\text{-}grt}$. At 19 GPa, $\theta_{grt\text{-}grt}$ decreases from 52 ± 3° to 44 ± 2° with temperature increasing from 1000 to 1200 °C (Figure 3a). At 1000 °C, $\theta_{grt\text{-}grt}$ decreases from 55 ± 3° to 52 ± 3° with pressure increasing from 17 to 19 GPa, while at 1200 °C, $\theta_{grt\text{-}grt}$ decreases from 47 ± 2° to 44 ± 2° with pressure increasing from 17 to 19 GPa (Figure 3b).

As shown in Table 2, stishovite is the main second phase (4–14 wt.%) in the run products. Therefore, the dihedral angles of fluid-stishovite-stishovite and/or fluid-stishovite-garnet should also be measured, in order to fully evaluate the connectivity of aqueous fluids. However, we found that stishovite crystals usually have open grain boundaries, so that the dihedral angles of fluid-stishovite-stishovite or fluid-stishovite-garnet cannot be determined in this study. But considering that majoritic garnet is the predominant phase in the deeply subducted slab, we believe that the effect of presence of a second phase (stishovite in this study) on the understanding of the connectivity of fluids in the deeply subducted slab may not be significant, although this speculation needs confirmation in future studies.

4. Discussion

4.1. Attainment of Equilibrium

It is important to establish whether the textural equilibrium was attained among the run products before evaluating the connectivity of aqueous fluids based on the measured dihedral angles. No time series experiments were conducted in this study, but previous studies suggest that a run duration of 23 hr at 900 °C in the aqueous fluid-pyrope system is sufficient to attain textual equilibrium for the valid measurements of aqueous fluid-pyrope-pyrope dihedral angles (Ono et al., 2002). Yoshino et al. (2007) show that in the aqueous fluid-olivine system, textural equilibrium can be approached within 6 hr at 1200 °C for the measurements of aqueous fluid-olivine-olivine dihedral angles. The temperatures in our experiments are 1000 to 1200 °C, and all the experiments, except for run DHL-10 at 1200 °C, were run for 24 hr (Table 2). The run duration of DHL-10 at 1200 °C is 13 hr. Therefore, our experiments should all have approached the textural equilibrium and our measured $\theta_{\text{grt-grt}}$ should be valid. Further evidence for the equilibrium of our experiments raised from mineral morphology and mineral compositions. As shown in Figure 1a, many garnet-garnet-garnet triple junctions have intersection angles of ~120°, indicating the achievement of textural equilibrium and a relatively low orientation dependence of the grain boundary energy (Matsukage et al., 2017). The compositional homogeneity of the garnet crystals in an individual run (Table 3) also implies that both chemical and textual equilibrium has been achieved. In addition, the systematic negative correlation between $\theta_{\text{grt-grt}}$, temperature, and pressure, as shown in Figure 3, may not be obtained without the approach of equilibrium.

In the double capsule technique, the equilibrium in H_2 fugacity between sample in the inner Au sample capsule and the external oxygen buffer can be established within a few hours at temperatures between 700 and 1200 °C (Chou, 1987; Li & Keppler, 2014). Considering that all the buffer materials (Ni-NiO-H_2O) were present in the space between the inner Au capsule and the outer Pt capsule, and considering that in the inner Au capsule a free fluid phase was also present, the oxygen fugacity prevailing in the sample should be close to the Ni-NiO buffer. However, since a considerable amount of silicates must have been dissolved in the fluid phase, the water activity in the inner Au capsule should be slightly less than one. This would cause the sample oxygen fugacity slightly lower than the Ni-NiO buffer, but the sample oxygen fugacity should still well correspond to the oxygen fugacity of the subduction zone fluids (McCammon et al., 2004; Wood et al., 1990).

4.2. Comparison With Previous Studies

Previous studies focused on the dihedral angles in calcite-, quartz-, feldspar-, olivine-, garnet-, and clinopyroxene-dominated rocks at temperatures of 600–1200 °C and pressures of 0.1–16 GPa (Brenan & Watson, 1988; Holness, 1993; Holness & Graham, 1991; Matsukage et al., 2017; Mibe et al., 1998, 1999, 2003; Ono et al., 2002; Wanamaker & Kohlstedt, 1991; Watson et al., 1991; Watson & Brenan, 1987; Yoshino et al., 2002, 2007). Since our present study mainly focuses on the wetting properties of aqueous fluids in mafic mineral dominated subduction zone rocks, we only compared our measured dihedral angles with those obtained from the aqueous fluid-mafic mineral systems (Matsukage et al., 2017; Mibe et al., 1998, 1999, 2003; Ono et al., 2002; Watson et al., 1991; Yoshino et al., 2007).

In Figure 4, the new $\theta_{\text{grt-grt}}$ data reported here are plotted together with the available dihedral angle data obtained in olivine-, clinopyroxene-, and garnet-dominated systems. It can be seen from Figure 4 that the decrease of $\theta_{\text{grt-grt}}$ with increasing *P-T* (see also Figure 3) is in good agreement with the previously observed linear variation of $\theta_{\text{oliv-oliv}}$ with *P-T*. The observed linear reduction in $\theta_{\text{oliv-oliv}}$ with increasing *P-T* is usually attributed to the increased solubility of silicates in the aqueous fluids with increasing *P-T* (e.g., Mibe et al., 1999; Takei & Shimizu, 2003; Yoshino et al., 2007). Therefore, the silicate concentration in an aqueous fluid that is in equilibrium with a basalt at high *P-T* conditions, as investigated in this study, may also increase with increasing *P-T*, which thus can explain the observed reduction in $\theta_{\text{grt-grt}}$ with increasing *P-T* in this study.

However, the $\theta_{\text{grt-grt}}$ determined by Ono et al. (2002) and by Matsukage et al. (2017) increases with increasing pressure at pressures lower than 12 GPa. This is in big contrast with the observed reduction in $\theta_{\text{oliv-oliv}}$ with increasing pressure. More interestingly, our new $\theta_{\text{grt-grt}}$ data combined with the $\theta_{\text{grt-grt}}$ data from Ono et al. (2002) and Matsukage et al. (2017) show that $\theta_{\text{grt-grt}}$ first increases to a maximum of ~65° as pressure increases to ~12 GPa but then drops to below ~44° as pressure increases further to 19 GPa (Figure 4b). The increase of $\theta_{\text{grt-grt}}$ with increasing pressure contradicts the expectation that a higher pressure leads to a lower dihedral angle due to the increased silicate solubility in the aqueous fluids. However, a similar

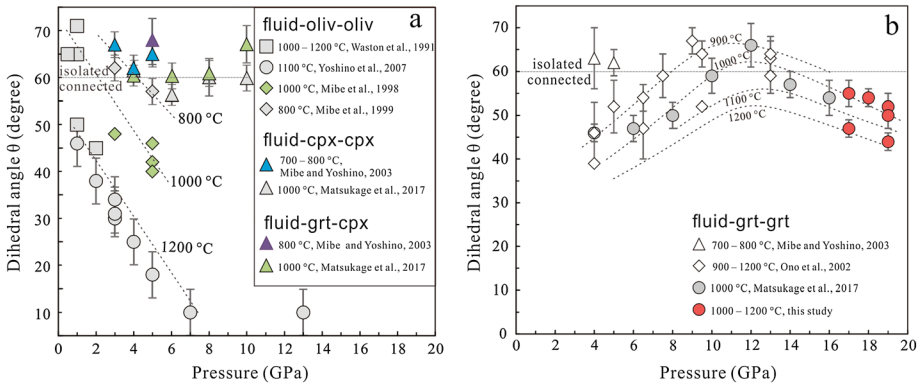

Figure 4. A summary of dihedral angles determined in the H_2O-olivine system and H_2O-garnet system. The error bars are not available in Watson et al. (1991) and Mibe et al. (1998). Dihedral angles at (a) the fluid-oliv-oliv, fluid-cpx-cpx, fluid-grt-cpx and (b) fluid-grt-grt triple junctions in previous studies and this study indicate that the fluid connectivity in the subducting slabs is mainly controlled by the oceanic crust as the dihedral angle in H_2O-olivine system (peridotite part) deceases quickly with increasing pressure and temperature. As shown in (b), the dihedral angle in H_2O-garnet system increases at the upper mantle conditions (<12 GPa) but decreases at the MTZ conditions (>13 GPa). Note that the dotted lines/curves are used to guide the eyes.

linear variation of dihedral angle with pressure was indeed observed previously by Holness (1993), in the aqueous fluid-quartz system. Holness (1993) found that at 1000 °C, increasing pressure from ~0.2 to ~0.8 GPa would cause a linear increase of the aqueous fluid-quartz-quartz dihedral angle $\theta_{\text{qrtz-qrtz}}$ from ~75 to ~83°, but at pressures from ~0.8 to ~0.95 GPa, the $\theta_{\text{qrtz-qrtz}}$ drops linearly from ~83 to ~72°. Holness (1993) also showed a similar observation in the same aqueous fluid-quartz system at 600 °C. The suggested explanation for the variation of $\theta_{\text{qrtz-qrtz}}$ with pressure was that the presence of an absorbed layer of water on the fluid-quartz interface and the quartz grain boundary may change the interfacial energy and cause the abrupt change of the dihedral angle. It is not clear whether the same explanation can be applied here to the aqueous fluid-garnet system, but the similar observation in the aqueous fluid-quartz system implies that the presently observed variation of $\theta_{\text{grt-grt}}$ with pressure (Figure 4b) is true.

Another potential explanation for the variation of $\theta_{\text{grt-grt}}$ with pressure is the variation of composition of garnet. As shown in many previous studies (e.g., Aoki & Takahashi, 2004; Irifune et al., 1986), the composition of garnet changes in the pressure range of 5–16 GPa but is almost constant at pressures above 16 GPa (this study). The composition change may plausibly change the surficial energy of garnet and results in the increase of $\theta_{\text{grt-grt}}$ with increasing pressure. However, as found by Matsukage et al. (2017), the $\theta_{\text{grt-grt}}$ data obtained from the pyrope + H_2O system (Ono et al., 2002) agree well with their data obtained from the complex basalt-H_2O system. Therefore, the effect of mineral composition on $\theta_{\text{grt-grt}}$ might be small. Obviously, much more detailed work is required in the future to better understand the mechanism causing the variation of $\theta_{\text{grt-grt}}$ with pressure.

The dihedral angle in a solid-H_2O system can in principle be predicted by the theoretical lattice-like model (Shimizu & Takei, 2005; Takei & Shimizu, 2003). However, we noticed that the lattice-like model by Takei and Shimizu (2003) was built upon the basis that the dihedral angle in a silicate-H_2O system decreases with solid concentration in the fluid phase. However, this basis is not consistent with the observed variation of $\theta_{\text{grt-grt}}$ with pressure (Figure 4b), as discussed above. In addition, Takei and Shimizu (2003) clearly pointed out that their model can only be used for simple solid-H_2O two-component system, such as quartz-H_2O system, and the application of their model to complex systems, such as forterite-H_2O system or rock-H_2O system, is problematic. Consequently, the Takei and Shimizu (2003) model cannot be used to predict the variation of $\theta_{\text{grt-grt}}$ with temperature and/or pressure in our complex basalt-H_2O system.

4.3. Implications for Water Cycle in Subduction Zones and Hydration of the MTZ

The high solubility of water in the MTZ minerals wadsleyite and ringwoodite indicates that the MTZ may be very wet (Demouchy et al., 2005; Inoue et al., 1995; Kohlstedt et al., 1996; Litasov & Ohtani, 2003; Ohtani et al., 2000). The strongest evidence for a hydrous MTZ is the observation that ringwoodite hosted in ultradeep

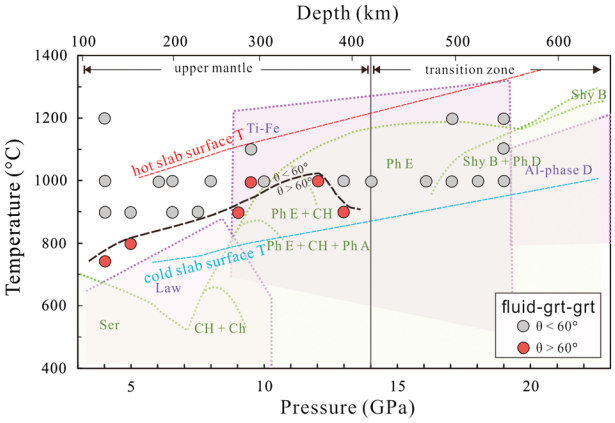

Figure 5. The aqueous fluid-garnet-garnet dihedral angle $\theta_{grt\text{-}grt}$ in *P-T* space, and the hydrous phase stability fields in the hydrous basalt (dotted purple line) and the hydrous peridotite (dotted green line) systems. The gray and red circles denote the $\theta_{grt\text{-}grt}$ smaller than 60° and greater than 60°, respectively, which are separated by the dashed black curve. The dihedral angle data are taken from Figure 4b. The dashed blue and red lines represent the global range of slab surface temperature, respectively, extrapolated from Syracuse et al. (2010). The hydrous phase stability fields in the hydrous basalt and the hydrous peridotite systems were modified from Okamoto and Maruyama (2004), Kawamoto (2006), and Nishihara and Matsukage (2016). Abbreviations are Law = lawsonite; Fe-Ti = iron-titanium oxyhydroxides; Ser = serpentine; CH = clinohumite; Ch = chondrodite; Ph A = phase A; Ph E = phase E; Ph D = phase D; Shy B = superhydrous phase B.

diamonds from Juina, Brazil, contains up to 1–2 wt.% water (Pearson et al., 2014). Nestola and Smyth (2016) estimated that the MTZ may contain up to 28% of the Earth's total water. If these studies are correct, then one interesting research theme is how the MTZ was hydrated. Due to the stabilization of hydrous minerals at different pressures corresponding to the subducting slab (see Figure 5; Bolfan-Casanova, 2005; Hirschmann, 2006; Karato et al., 2013; Kawamoto, 2006; Nishihara & Matsukage, 2016; Ohtani, 2005, 2015; Schmidt & Poli, 1998), it is now widely accepted that water can be transported into the deep mantle by hydrous minerals in the subducting slab and that the water released finally by the breakdown of these hydrous minerals may hydrate the MTZ.

Hydrous minerals in the subducting slab can bring water to the deep Earth. However, whether the aqueous fluids formed by the breakdown of hydrous minerals in the subducting slab can be segregated from the slab and available to hydrate the overlying mantle depends significantly on the permeability of aqueous fluids in the subducting slab rocks. The significant decrease of $\theta_{oliv\text{-}oliv}$ with increasing *P-T* (Figure 4a) indicates that aqueous fluids released from the breakdown of hydrous minerals such as serpentine and phase A (Figure 5) can form interconnected network and flow on the grain edges in the peridotite part of the subducting slab. But whether the released fluids in the peridotite of the subducting slab can percolate through the overlying layer of oceanic crust and hydrate the mantle wedge would mainly depend on the connectivity of aqueous fluids in the subducting oceanic crust.

Figure 5 shows that aqueous fluids probably cannot form interconnected network in a relatively cold oceanic crust at pressures below 14 GPa but can form interconnected network in a relatively hot oceanic crust. Therefore, in a cold slab, the aqueous fluids formed by the breakdown of hydrous minerals, such as lawsonite, clinohumite, and phase A (Figure 5), could be trapped as interstitial fluids in the subducting oceanic crust, although these fluids can flow on the grain edges in the peridotite layer of the subducting slab. Therefore, these fluids could be retained physically in the subducting oceanic crust and transported into the deep mantle at pressures above 14 GPa. However, at 15–20 GPa corresponding to pressures of the MTZ, the $\theta_{grt\text{-}grt}$ appears to be lower than 60° even for a very cold slab, indicating that the aqueous fluids can flow on the grain edges of the subducting oceanic crust and be available to hydrate the overlying MTZ. Accordingly, in a cold slab, the aqueous fluids at the MTZ conditions, including those trapped physically in the slab and those formed lately by the breakdown of hydrous minerals at very high pressures (Figure 5), can eventually be segregated from the subducting oceanic crust and hydrate the MTZ. This may thus provide an important but hitherto unappreciated mechanism for the hydration of the MTZ.

In contrast, if the slab is hot, most of the aqueous fluids formed at shallow depth cannot be retained physically in the subducting oceanic crust due to the low $\theta_{grt\text{-}grt}$ (Figure 5); therefore, only the water stored in the hydrous minerals, such as iron-titanium oxyhydroxides, phase E, and phase D, can be transported into the MTZ depth (Figure 5). Since $\theta_{grt\text{-}grt}$ is lower than 60° in a hot slab at the MTZ conditions, the breakdown of these hydrous minerals at the MTZ conditions also produces aqueous fluids that can percolate through the subducting oceanic crust and hydrate the MTZ. However, it should be noted that the total mass of the available aqueous fluids in a hot slab to hydrate the MTZ should be considerably smaller than that in a cold slab. In a hot slab, most of hydrous minerals are dehydrated at shallow depths and the formed fluids are readily lost into the overlying mantle wedge due to the low $\theta_{grt\text{-}grt}$ value ($< 60°$; Figure 5), but in a cold slab less hydrous minerals are dehydrated at shallow depth and the formed aqueous fluids can be trapped physically in the subuducting oceanic crust and transported into the MTZ depth. Therefore, the cold slab and the hot slab may play a distinct role in transportation of water into the MTZ, causing heterogeneous distribution of water in the MTZ, as inferred from electrical conductivity measurements, for example (Huang et al., 2005; Karato et al., 2013).

The low $\theta_{grt\text{-}grt}$ values (<60°) at pressures corresponding to MTZ (Figure 5) also implies that all the aqueous fluids, no matter they are trapped physically in the slab at depth above the MTZ or formed by the breakdown of hydrous minerals at the MTZ depth, cannot be subducted into the lower mantle, so that the MTZ may potentially play as a *filter* of free aqueous fluids in the subducting slab.

Here it should be further noted that in the subducting slab, aqueous fluids can also be mobilized as channelized fluid flow along cracks, veins, shear zones, or fold hinges (e.g., Manea et al., 2014; Zack & John, 2007). However, it remains unknown which mechanism, channelized fluids along cracks or fluid permeability controlled by dihedral angle, is the dominated mechanism for fluid mobility in the subducting slab, in particular at pressures beyond the sub-arc depth. Following many previous studies (e.g., Matsukage et al., 2017; Mibe et al., 1999, 2003; Ono et al., 2002), we consider that the dihedral angle is at least one of the most important factors controlling fluid mobility in the subducting slab.

5. Conclusions

This study reports the first data on aqueous fluid-majoritic garnet-majoritic garnet dihedral angle in a hydrous basaltic system at the MTZ conditions (17–19 GPa and 1000–1200 °C). The dihedral angle $\theta_{grt\text{-}grt}$ is less than 60° and decreases with increasing pressure and temperature. These experimental results demonstrate that aqueous fluids can percolate through the subducting oceanic crust at the MTZ conditions. Considering that aqueous fluids cannot percolate through the subducting oceanic crust in a cold slab at depth above the MTZ, due to the high dihedral angle ($\theta_{grt\text{-}grt} > 60°$), the aqueous fluids formed by the breakdown of slab hydrous minerals may be trapped as interstitial fluids in the slab and transported into the MTZ depth. At the MTZ depth, both the aqueous fluids trapped previously and the aqueous fluids formed lately by the breakdown of slab hydrous minerals can percolate through the subducting oceanic crust and be available for the hydration of the MTZ, which thus provides an important mechanism for the hydration of the MTZ. On the other hand, due to the low dihedral angle ($\theta_{grt\text{-}grt} < 60°$) of a hot subducting slab, most of the aqueous fluids formed by slab mineral dehydration may be lost into the overlying upper mantle at shallow depth, and only the aqueous fluids formed by the breakdown of hydrous minerals at the MTZ depth can be available for the hydration of the MTZ. Accordingly, the cold slab may transport more water than the hot slab to the hydration of the MTZ, providing an explanation for the observed heterogeneous distribution of water in the MTZ. Our results also imply that the MTZ may potentially play as a filter of free aqueous fluids in the subducting slab.

Acknowledgments

This work is supported by the Strategic Priority Research Program (B) of Chinese Academy of Sciences (XDB18000000, QYZDJ-SSW-DQC012, GIG135PY201601 and 2017VSA0001), NSFC (41573053), and JSPS (25247088). Constructive reviews by Michael Walter, Kenji Mibe, William Minarik, and an anonymous reviewer significantly improved this paper. We also thank Yu Nishihara and Alex Yang Yang for discussion, Changming Xing and Jintuan Wang for help with the electron microprobe analyses. The data used are listed in the tables, references, and supporting information. This is contribution IS-2557 from GIGCAS.

References

Aoki, I., & Takahashi, E. (2004). Density of MORB eclogite in the upper mantle. *Physics of the Earth and Planetary Interiors*, *143-144*, 129–143. https://doi.org/10.1016/j.pepi.2003.10.007

Bolfan-Casanova, N. (2005). Water in the Earth's mantle. *Mineralogical Magazine*, *69*(03), 229–257. https://doi.org/10.1180/0026461056930248

Brenan, J. M., & Watson, E. B. (1988). Fluids in the lithosphere: 2. Experimental constraints on CO_2 transport in dunite and quartzite at elevated *P-T* conditions with implications for mantle and crustal decarbonation processes. *Earth and Planetary Science Letters*, *91*(1-2), 141–158. https://doi.org/10.1016/0012-821X(88)90157-4

Chou, I.-M. (1987). Oxygen buffer and hydrogen sensor techniques at elevated pressures and temperatures. In G. C. Ulmer & H. L. Barnes, Jr. (Eds.), *Hydrothermal experimental techniques* (pp. 61–99). New York: Wiley.

Demouchy, S., Deloule, E., Frost, D. J., & Keppler, H. (2005). Pressure and temperature-dependence of water solubility in Fe-free wadsleyite. *American Mineralogist*, *90*(7), 1084–1091. https://doi.org/10.2138/am.2005.1751

Dixon, J. E., Dixon, T. H., Bell, D. R., & Malservisi, R. (2004). Lateral variation in upper mantle viscosity: Role of water. *Earth and Planetary Science Letters*, *222*(2), 451–467. https://doi.org/10.1016/j.epsl.2004.03.022

Frost, D. J. (2006). The stability of hydrous mantle phases. *Reviews in Mineralogy and Geochemistry*, *62*(1), 243–271. https://doi.org/10.2138/rmg.2006.62.11

Gale, A., Dalton, C. A., Langmuir, C. H., Su, Y. J., & Schilling, J. G. (2013). The mean composition of ocean ridge basalts. *Geochemistry, Geophysics, Geosystems*, *14*, 489–518. https://doi.org/10.1029/2012GC004334

Hirschmann, M. M. (2006). Water, melting, and the deep earth H_2O cycle. *Annual Review of Earth and Planetary Sciences*, *34*(1), 629–653. https://doi.org/10.1146/annurev.earth.34.031405.125211

Hirth, G., & Kohlstedt, D. L. (1996). Water in the oceanic upper mantle: Implications for rheology, melt extraction and the evolution of the lithosphere. *Earth and Planetary Science Letters*, *144*(1-2), 93–108. https://doi.org/10.1016/0012-821X(96)00154-9

Holness, M. B. (1993). Temperature and pressure-dependence of quartz aqueous fluid dihedral angles—The control of adsorbed H_2O on the permeability of quartzites. *Earth and Planetary Science Letters*, *117*(3–4), 363–377. https://doi.org/10.1016/0012-821x(93)90090-V

Holness, M. B. (2006). Melt-solid dihedral angles of common minerals in natural rocks. *Journal of Petrology*, *47*(4), 791–800. https://doi.org/10.1093/petrology/egi094

Holness, M. B., & Graham, C. M. (1991). Equilibrium dihedral angles in the system H_2O-CO_2-NaCl-calcite, and implications for fluid-flow during metamorphism. *Contributions to Mineralogy and Petrology*, *108*(3), 368–383. https://doi.org/10.1007/Bf00285944

Huang, X., Xu, Y., & Karato, S.-i. (2005). Water content in the transition zone from electrical conductivity of wadsleyite and ringwoodite. *Nature*, *434*(7034), 746–749. https://doi.org/10.1038/nature03426

Inoue, T., Yurimoto, H., & Kudoh, Y. (1995). Hydrous modified spinel, $Mg_{1.75}SiH_{0.5}O_4$—A new water reservoir in the mantle transition region. *Geophysical Research Letters*, *22*(2), 117–120. https://doi.org/10.1029/94GL02965

Irifune, T., Sekine, T., Ringwood, A. E., & Hibberson, W. O. (1986). The eclogite-garnetite transformation at high-pressure and some geophysical implications. *Earth and Planetary Science Letters*, *77*(2), 245–256. https://doi.org/10.1016/0012-821x(86)90165-2

Jurewicz, S. R., & Jurewicz, A. J. G. (1986). Distribution of apparent angles on random sections with emphasis on dihedral angle measurements. *Journal of Geophysical Research*, *91*(B9), 9277–9282. https://doi.org/10.1029/JB091iB09p09277

Karato, S.-i. (2011). Water distribution across the mantle transition zone and its implications for global material circulation. *Earth and Planetary Science Letters*, *301*(3-4), 413–423. https://doi.org/10.1016/j.epsl.2010.11.038

Karato, S.-I., Bercovici, D., Leahy, G., Richard, G., & Jing, Z. (2013). *The transition-zone water filter model for global material circulation: Where do we stand? Earth's Deep Water Cycle* (pp. 289–313). Washington, DC: American Geophysical Union. https://doi.org/10.1029/168GM22

Karato, S.-i., & Jung, H. (1998). Water, partial melting and the origin of the seismic low velocity and high attenuation zone in the upper mantle. *Earth and Planetary Science Letters*, *157*(3–4), 193–207. https://doi.org/10.1016/S0012-821X(98)00034-X

Katsura, T., Yamada, H., Nishikawa, O., Song, M., Kubo, A., Shinmei, T., et al. (2004). Olivine-wadsleyite transition in the system $(Mg,Fe)_2SiO_4$. *Journal of Geophysical Research*, *109*, B02209. https://doi.org/10.1029/2003JB002438

Kawamoto, T. (2006). Hydrous phases and water transport in the subducting slab. *Reviews in Mineralogy and Geochemistry*, *62*(1), 273–289. https://doi.org/10.2138/rmg.2006.62.12

Kelbert, A., Schultz, A., & Egbert, G. (2009). Global electromagnetic induction constraints on transition-zone water content variations. *Nature*, *460*(7258), 1003–1006. https://doi.org/10.1038/nature08257

Keppler, H. (2017). Fluids and trace element transport in subduction zones. *American Mineralogist*, *102*(1), 5–20. https://doi.org/10.2138/am-2017-5716

Kohlstedt, D. L., Keppler, H., & Rubie, D. C. (1996). Solubility of water in the alpha, beta and gamma phases of $(Mg,Fe)_{(2)}SiO_4$. *Contributions to Mineralogy and Petrology*, *123*(4), 345–357. https://doi.org/10.1007/s004100050161

Li, Y., & Keppler, H. (2014). Nitrogen speciation in mantle and crustal fluids. *Geochimica et Cosmochimica Acta*, *129*, 13–32. https://doi.org/10.1016/j.gca.2013.12.031

Litasov, K., & Ohtani, E. (2003). Stability of various hydrous phases in CMAS pyrolite-H_2O system up to 25 GPa. *Physics and Chemistry of Minerals*, *30*(3), 147–156. https://doi.org/10.1007/s00269-003-0301-y

Manea, V., Leeman, W. P., Gerya, T., Manea, M., & Zhu, G. (2014). Subduction of fracture zones controls mantle melting and geochemical signature above slabs. *Nature Communications*, *5*(1), 5095. https://doi.org/10.1038/ncomms6095

Matsukage, K. N., Hashimoto, M., & Nishihara, Y. (2017). Morphological stability of hydrous liquid droplets at grain boundaries of eclogite minerals in the deep upper mantle. *Journal of Mineralogical and Petrological Sciences*, *112*(6), 346–358. https://doi.org/10.2465/jmps.170309

Matsuzaka, K., Akaogi, M., Suzuki, T., & Suda, T. (2000). Mg-Fe partitioning between silicate spinel and magnesiowüstite at high pressure: Experimental determination and calculation of phase relations in the system Mg_2SiO_4-Fe_2SiO_4. *Physics and Chemistry of Minerals*, *27*(5), 310–319. https://doi.org/10.1007/s002690050260

McCammon, C. A., Frost, D. J., Smyth, J. R., Laustsen, H. M. S., Kawamoto, T., Ross, N. L., & van Aken, P. A. (2004). Oxidation state of iron in hydrous mantle phases: Implications for subduction and mantle oxygen fugacity. *Physics of the Earth and Planetary Interiors*, *143-144*, 157–169. https://doi.org/10.1016/j.pepi.2003.08.009

Mibe, K., Fujii, T., & Yasuda, A. (1998). Connectivity of aqueous fluid in the Earth's upper mantle. *Geophysical Research Letters*, *25*(8), 1233–1236. https://doi.org/10.1029/98GL00872

Mibe, K., Fujii, T., & Yasuda, A. (1999). Control of the location of the volcanic front in island arcs by aqueous fluid connectivity in the mantle wedge. *Nature*, *401*(6750), 259–262. https://doi.org/10.1038/45762

Mibe, K., Yoshino, T., Ono, S., Yasuda, A., & Fujii, T. (2003). Connectivity of aqueous fluid in eclogite and its implications for fluid migration in the Earth's interior. *Journal of Geophysical Research*, *108*(B6), 2295. https://doi.org/10.1029/2002JB001960

Nestola, F., & Smyth, J. R. (2016). Diamonds and water in the deep Earth: A new scenario. *International Geology Review*, *58*(3), 263–276. https://doi.org/10.1080/00206814.2015.1056758

Nishihara, Y., & Matsukage, K. N. (2016). Iron-titanium oxyhydroxides as water carriers in the Earth's deep mantle. *American Mineralogist*, *101*(4), 919–927. https://doi.org/10.2138/am-2016-5517

Ohtani, E. (2005). Water in the mantle. *Elements*, *1*(1), 25–30. https://doi.org/10.2113/gselements.1.1.25

Ohtani, E. (2015). Hydrous minerals and the storage of water in the deep mantle. *Chemical Geology*, *418*(418), 6–15. https://doi.org/10.1016/j.chemgeo.2015.05.005

Ohtani, E., Mizobata, H., & Yurimoto, H. (2000). Stability of dense hydrous magnesium silicate phases in the systems Mg_2SiO_4-H_2O and $MgSiO_3$-H_2O at pressures up to 27 GPa. *Physics and Chemistry of Minerals*, *27*(8), 533–544. https://doi.org/10.1007/s002690000097

Okamoto, K., & Maruyama, S. (2004). The eclogite–garnetite transformation in the MORB+H_2O system. *Physics of the Earth and Planetary Interiors*, *146*(1-2), 283–296. https://doi.org/10.1016/j.pepi.2003.07.029

Ono, S., Mibe, K., & Yoshino, T. (2002). Aqueous fluid connectivity in pyrope aggregates: Water transport into the deep mantle by a subducted oceanic crust without any hydrous minerals. *Earth and Planetary Science Letters*, *203*(3–4), 895–903. https://doi.org/10.1016/S0012-821X(02)00920-2

Pearson, D., Brenker, F., Nestola, F., McNeill, J., Nasdala, L., Hutchison, M., et al. (2014). Hydrous mantle transition zone indicated by ringwoodite included within diamond. *Nature*, *507*(7491), 221–224. https://doi.org/10.1038/nature13080

Riegger, O., & Vanvlack, L. (1960). Dihedral angle measurement. *Transactions of the American Institute of Mining and Metallurgical Engineers*, *218*(5), 933–935.

Schmidt, M. W., & Poli, S. (1998). Experimentally based water budgets for dehydrating slabs and consequences for arc magma generation. *Earth and Planetary Science Letters*, *163*(1–4), 361–379. https://doi.org/10.1016/S0012-821x(98)00142-3

Shimizu, I., & Takei, Y. (2005). Temperature and compositional dependence of solid-liquid interfacial energy: Application of the Cahn-Hilliard theory. *Physica B*, *362*(1–4), 169–179. https://doi.org/10.1016/j.physb.2005.02.008

Stickels, C. A., & Hucke, E. (1964). Measurement of dihedral angles. *Transactions of the Metallurgical Society of AIME*, *230*(4), 795–801.

Syracuse, E. M., van Keken, P. E., & Abers, G. A. (2010). The global range of subduction zone thermal models. *Physics of the Earth and Planetary Interiors*, *183*(1-2), 73–90. https://doi.org/10.1016/j.pepi.2010.02.004

Takei, Y., & Shimizu, I. (2003). The effects of liquid composition, temperature, and pressure on the equilibrium dihedral angles of binary solid–liquid systems inferred from a lattice-like model. *Physics of the Earth and Planetary Interiors*, *139*(3-4), 225–242. https://doi.org/10.1016/j.pepi.2003.08.004

Wanamaker, B. J., & Kohlstedt, D. L. (1991). The effect of melt composition on the wetting angle between silicate melts and olivine. *Physics and Chemistry of Minerals*, *18*(1), 26–36.

Watson, E. B. (1982). Melt infiltration and magma evolution. *Geology*, *10*(5), 236–240. https://doi.org/10.1130/0091-7613(1982)10%3C236:MIAME%3E2.0.CO;2

Watson, E. B., & Brenan, J. M. (1987). Fluids in the lithosphere.1. Experimentally-determined wetting characteristics of CO_2-H_2O fluids and their implications for fluid transport, host-rock physical-properties, and fluid inclusion formation. *Earth and Planetary Science Letters*, *85*(4), 497–515. https://doi.org/10.1016/0012-821X(87)90144-0

Watson, E. B., Brenan, J. M., & Baker, D. R. (1991). Distribution of fluids in the continental mantle. *Continental Mantle*, *111-125*.

Watson, E. B., & Lupulescu, A. (1993). Aqueous fluid connectivity and chemical-transport in clinopyroxene-rich rocks. *Earth and Planetary Science Letters*, *117*(1–2), 279–294. https://doi.org/10.1016/0012-821X(93)90133-T

Wood, B. J., Bryndzia, L. T., & Johnson, K. E. (1990). Mantle oxidation-state and its relationship to tectonic environment and fluid speciation. *Science*, *248*(4953), 337–345. https://doi.org/10.1126/science.248.4953.337

Yoshino, T., Mibe, K., Yasuda, A., & Fujii, T. (2002). Wetting properties of anorthite aggregates: Implications for fluid connectivity in continental lower crust. *Journal of Geophysical Research*, *107*(B1), 2027. https://doi.org/10.1029/2001JB000440

Yoshino, T., Nishihara, Y., & Karato, S.-i. (2007). Complete wetting of olivine grain boundaries by a hydrous melt near the mantle transition zone. *Earth and Planetary Science Letters*, *256*(3-4), 466–472. https://doi.org/10.1016/j.epsl.2007.02.002

Yoshino, T., Price, J. D., Wark, D. A., & Watson, E. B. (2006). Effect of faceting on pore geometry in texturally equilibrated rocks: Implications for low permeability at low porosity. *Contributions to Mineralogy and Petrology*, *152*(2), 169–186. https://doi.org/10.1007/s00410-006-0099-y

Zack, T., & John, T. (2007). An evaluation of reactive fluid flow and trace element mobility in subducting slabs. *Chemical Geology*, *239*(3-4), 199–216. https://doi.org/10.1016/j.chemgeo.2006.10.020

Zhang, J., Li, B., Utsumi, W., & Liebermann, R. (1996). In situ X-ray observations of the coesite-stishovite transition: Reversed phase boundary and kinetics. *Physics and Chemistry of Minerals*, *23*(1), 1–10.